



Compression after high-velocity impact behavior of pseudo-elastic shape memory alloy embedded glass/epoxy composite laminates

Luv Verma^a, J. Jefferson Andrew^{a,b}, Srinivasan M. Sivakumar^a, G. Balaganesan^c, S. Vedantam^d, Hom N. Dhakal^{e,*}

^a Department of Applied Mechanics, IIT Madras, Chennai 600036, India

^b Department of Mechanical Engineering, Masdar Campus, Khalifa University, Abu Dhabi, United Arab Emirates

^c Department of Mechanical Engineering, IIT Jammu, J&K 181 221, India

^d Department of Engineering Design, IIT Madras, Chennai 600036, India

^e School of Mechanical and Design Engineering, Anglesea Road, Anglesea Building, University of Portsmouth, PO1 3DJ, UK

ARTICLE INFO

Keywords:

Pseudo-elastic shape memory alloys (PE-SMA)
High-velocity impact
Digital image correlation (DIC)
Compression after impact (CAI)
Glass/epoxy
Composite laminates

ABSTRACT

The compression after high-velocity impact (CAI) behavior of pseudo-elastic shape memory alloy (PE-SMA) embedded glass/epoxy composite laminates manufactured via vacuum-assisted resin infusion (VARI) technique was investigated experimentally. High-velocity impact tests were performed on the glass/epoxy composites using an in-house build gas-gun set-up at four different velocities (70, 85, 95, and 105 m/s). To elucidate, the series of damage events undergone on the composites under the high-velocity impact, a high-speed camera was used. Quasi-static compression-after-impact (CAI) tests were performed to evaluate the damage tolerance of different composites subjected to high-velocity impact. Real-time damage progression during the CAI as well as the extent of damage was characterized by using a 2D Digital Image Correlation (DIC) technique. Three different types of embedment configurations of PE-SMA wire, namely, with length variation (35, 70, and 150 mm) and also with and without anchors, were used. The impact test results show that the ballistic limit of anchored PE-SMA composites with an embedment length of 35 mm is 72.72% higher than that of the homogeneous glass/epoxy composites. CAI results indicate that the PE-SMA based composites have better damage tolerance with respect to the homogeneous ones at 70 m/s. In contrast, at higher velocities, the delamination area decreases in the homogenous glass/epoxy composites due to more localized damage and present a higher compressive strength.

1. Introduction

In the past few decades, research has established the prowess of composite laminates over the traditional metals due to their high stiffness and strength to weight ratios, improved fatigue endurance, corrosion resistance and design flexibility. They have outmatched metals when it comes to applications where stress dominates in the direction of the primary fibers in the structural element. These composites that render the above advantages should also be equally resistant to impact conditions that occur in the lifetime of their usage (for example, bird strikes, tool drop, collisions with floating debris, docks, and particle impact on propeller blades and wind turbine blades) [1–3]. Assessment of the performance of the composites during the impact events and quantification of energy dissipation vis-a-vis metals will help in designing better composites. Unlike metals that exhibit good isotropy,

complexities in the assessment occur because of the numerous failure modes possible in a composite material. Early studies on the impact behavior of the composites point to their low energy absorption capabilities [1,2].

In composite laminates; under the impact loading, energy absorption occurs through numerous failure modes such as matrix cracking, debonding, fiber pull-out, penetration, and fiber fracture [4–7]. In the past, researchers have investigated the effect of employing different kinds of fiber systems such as aramid, carbon, and glass fibers with different lay-ups for composite manufacturing. They have evaluated the energy absorption capabilities by embedding different materials in composites [8–12]. Though optimal fiber geometry and fiber material properties may improve the energy absorption capabilities to a certain extent, it still suffers from less energy absorption since fibers fail at relatively low strain levels [13]. To solve the need for higher energy

* Corresponding author.

E-mail address: hom.dhakal@port.ac.uk (H.N. Dhakal).

absorption under the impact, materials with good ductility has to be embedded. One such material that has a high failure strain and self-centering properties is pseudoelastic shape memory alloy (PE-SMA) [14–16]. PE-SMAs are highly ductile alloys with high endurance in the plastic deformation regime. This behavior of PE-SMA has attributed to the phase transformation mechanisms that occur internally under thermomechanical loading [17–19]. Thus, PE-SMA embedded composite has expected to serve well in such applications compared to conventional composite structures where resistance to penetration and damage during ballistic impact critically affects the design [20–24].

Earlier studies on hybrid SMA-graphite composite laminates reveal an increase in the absorbed energy and peak impact force with a reduction in impact damage under low-velocity impacts [25–27]. At high-velocities, composite samples embedded with SMA show promise in terms of perforation toughness [28]. In its wire form, if laid bi-directionally, SMA composites show a negative effect leading to an increase in damage area when compared to unidirectional SMA during impact tests [29]. With the increase in energy absorption, many researchers have tried to reduce the damage in the samples using the embedment of SMA. Researchers have stitched SMA into the composites to reduce the risk of delamination [26]. Different surface treatment techniques, such as chemical oxidizing and wetting of the SMA surface, have been employed to increase bonding with matrix [20,30–32]. Though these methods improve surface properties to a certain extent, their effectiveness reduces, once debonding between the SMA and composite initiates at the impact point.

After impacting composites with SMA embedded as secondary reinforcements, failure in compression is an important phenomenon to be looked at carefully. Residual strength determination is a critical parameter after performing an impact as it gives an idea about how much weakness has induced due to impact load [33]. Many researchers have investigated the compressive strength of the composites after impact (CAI). Physical attributes such as impact location, area, and aspect ratio of damage due to impact load have shown to affect the residual compressive strength of composites [34]. Regarding the failure modes, damage appears to be initiated by the interlaminar failure in the impacted region. This damage extends in the form of local buckling and delamination in the sample [35]. Crack growth occurs from the impact damage zone [36,37]. The increase in the delamination area reduces buckling stresses and residual compressive strength, leading to failure [38,39]. The investigation of SMA embedded GFRP under compression after impact is still in the nascent stage.

Though work has performed under low-velocity impact regime, there is scant information available in the literature on composites under the high-velocity impact. At high velocities, impact perforation becomes localized. Due to this, the failure modes also change. SMA embedment introduces additional SMA failure modes at high-velocity impact. The effect on the conventional failure modes due to SMA embedment has not been widely studied. Limited literature is available on the prediction of residual properties such as compression after impact (CAI) at high velocities. Moreover, there are very few reported work available for SMA hybrid composites at high-velocity impact and how embedment affects the ultimate compressive failure strength of the composite.

Thus, in this work, the energy absorption characteristics and residual compressive properties of PE-SMA embedded glass/epoxy composite laminates have been investigated under high-velocity impact loadings. Bi-directional woven GFRP has been used as a parent material to embed PE-SMA [40]. Three different types of embedment configurations of PE-SMA wire, with length variation and also with and without anchors, have been employed. To elucidate, the series of damage events undergone on the composites, a high-speed camera was used. After impact, compression tests have been carried out to find out the residual failure strength and how compression failure modes vary spatially. To better understand, the effect of length variation

and anchors on energy absorption, a digital image correlation (DIC) study has conducted in quasi-static conditions.

2. Experimental procedure

2.1. Material and fabrication

Woven roving mat (WRM) glass fiber of areal density 360 g/m^2 was used as primary reinforcement and pseudoelastic shape memory alloy (PE-SMA), which is a NiTi alloy (i.e. 50% of NiTi) of diameter 0.5 mm, was used as secondary reinforcement. Epoxy resin (LY556) and hardener (HY951) were used as matrix material in the weight ratio of 10:1. Tables 1–3 summarize the properties of PE-SMA, glass fiber, and epoxy, respectively. Sample configurations are represented in Fig. 1. PE-SMA was embedded in three different configurations in the composite laminates. The laminates were prepared using six layers of glass fibers and PE-SMA was embedded at the mid-plane of the laminate. The stacking sequence of the fiber mat and PE-SMA is shown in Fig. 1S. The distance between PE-SMA wires were kept approximately 4 mm such that a projectile can hit the wire in the primary impact region. Samples were prepared by the vacuum assisted resin infusion process. The laminates were allowed to cure for 24 h under the vacuum pressure of 30 mm Hg. The samples of dimension $150 \times 150 \text{ mm}$ were cut out using abrasive water-jet cutting. The weight percentage of PE-SMA was considered to be a maximum of 1% of the fiber weight.

Table 4 summarizes the nomenclature of different samples considered in this study. In Type II, III, and IV samples, the PE-SMA wires were laid in between the GFRP layers as shown in Fig. 1S. Type II and III samples were anchored, which means the PE-SMA wires were continuous and turned into U-shape at the ends so that they act as restrainers. The embedded PE-SMA length in Type II and Type III samples were 35 and 70 mm, respectively. In Type IV, four straight wires were laid without any connections between them. These changes in the configurations were done to find out the effect of anchored and unanchored configurations on energy absorption and failure modes of the GFRP composite laminates. The thickness of the samples was around $(3.15 \pm 0.2 \text{ mm})$.

2.2. High-velocity impact tests

High-velocity impact tests were conducted on the GFRP samples using a gas-gun, as shown in Fig. 2, at four different velocities (70, 85, 95, and 105 m/s). For each testing condition, four samples were tested. The target laminates were clamped from all four sides. A pro-

Table 1
Material properties of PE-SMA.

S. No.	Properties	Values (PE-SMA)	Units
1	E_{aus}	80	GPa
2	E_{mar}	40	GPa
3	Poisson's ratio	0.3	
4	Density	6800	Kg-m^3
5	Yield stress	800	MPa

Table 2
Material properties of glass fibers.

S. No.	Properties	Values (PE-SMA)	Units
1	Young's modulus	76.6	GPa
2	Specific modulus	0.0340	$\text{GPa-m}^3/\text{Kg}$
3	Specific strength	0.6200	$\text{MPa-m}^3/\text{Kg}$
4	Poisson's ratio	0.25	

jectile of dia. 7 mm and mass 9 g was used to impact the clamped samples. The impact events were captured using two high-speed cameras of Phantom V611 at 50,000 fps. One of the cameras was used to measure the velocity of the projectile. The other camera was employed to capture the progression of damage in the GFRP samples. To calculate

the delamination damage area of different samples Image J software was used.

2.3. Compression after impact test with digital image correlation (DIC)

INSTRON 8801 universal testing machine (UTM) of capacity 100 kN was used to perform quasi-static compression tests. Cross-head speed was maintained at 1 mm/min. Fig. 3(a) shows the ASTM D7137M-12 CAI test fixture. To find out how damage profile varies in different GFRP configurations, the compression tests have been conducted along with digital image correlation (DIC). While performing the compression tests, images were acquired using image acquisition software Vic-Snap 2010 with a charge-coupled device (CCD) camera, as shown in Fig. 3(b), having a resolution of 1920x1080 pixels (Prosilica GX1910). The images were captured at a rate of 25 fps.

Table 3
Material properties of epoxy.

S. No	Properties	Values	Units
1	Specific gravity	1.28	
2	Young's modulus	3.792	GPa
3	Poisson's ratio	0.30	

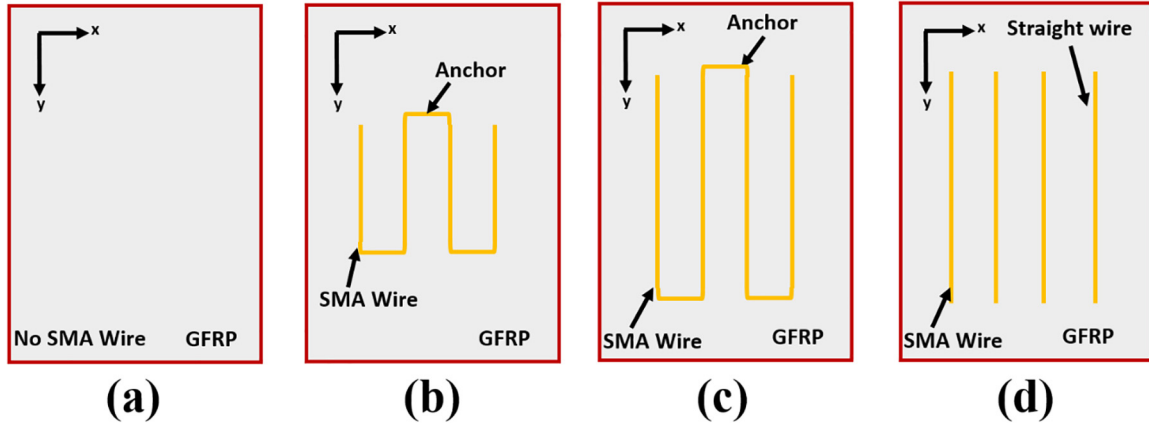


Fig. 1. Schematics of different composite samples considered in this study (a) Type-I (b) Type-II (c) Type-III and (d) Type-V.

Table 4
Configuration details of different samples.

S. No.	Configuration	Embedded PE-SMA length	Anchor types	Nomenclature
1.	Glass/epoxy (GFRP)	No SMA	Homogeneous	Type I
2.	35 mm SMA embedded GFRP	35 mm	Anchored	Type II
3.	70 mm SMA embedded GFRP	70 mm	Anchored	Type III
4.	150 mm SMA embedded GFRP	150 mm	Unanchored	Type IV



Fig. 2. Gas gun experimental set-up used for impact testing on the composite laminates.

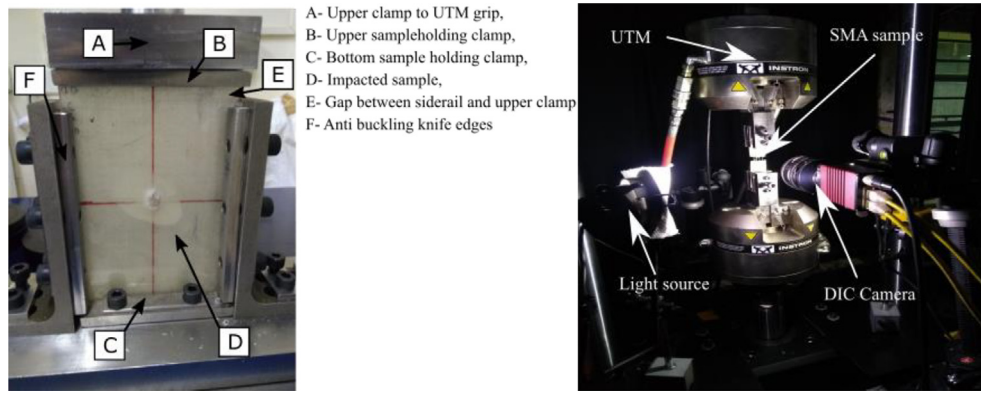


Fig. 3. (a) Compression after impact (CAI) test set-up (b) Digital image correlation (DIC) test method.

3. Results and discussions

3.1. Damage progression in PE-SMA embedded GFRP composites

The schematics of different SMA failure modes are shown in Fig. 4. When PE-SMA wire is embedded inside GFRP, energy absorption takes place predominantly due to SMA associated failure modes in addition to the conventional failure modes (matrix cracking, fiber/matrix debonding, fiber breakage, etc.). The SMA associated failure modes include SMA deformation, SMA anchor displacement, and SMA pull-out. In the presence of PE-SMA as a secondary reinforcement, these SMA failure modes get activated in a sequence. Fig. 4 shows the

sequence of failure modes in a PE-SMA embedded GFRP under high-velocity impact load.

Damage progression on the back face is shown using a high-speed camera, with Fig. 5(a), is the first image, which captures the frame when the projectile is about to hit the sample. As shown in Figs. 5 and 6, due to PE-SMA embedment, delamination progresses predominantly along with the SMA wire, which is generally not the case for homogeneous GFRP [41]. When a projectile impacts the composite and comes in contact with PE-SMA wire, it starts undergoing deformation, and the region away from the primary impact region encounters strain due to this deformation. The limiting strain value at which the PE-SMA wire displaces is lesser than that of the plastic strain and

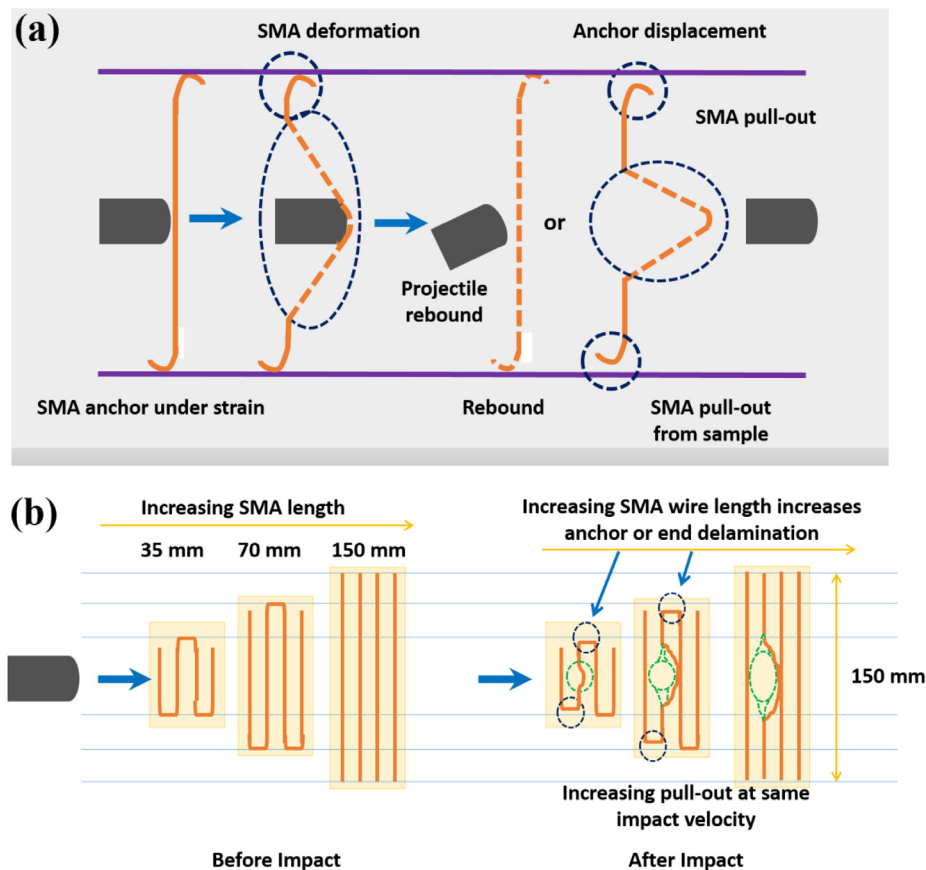


Fig. 4. Schematics showing (a) different SMA associated failure modes under high-velocity impact load (failure modes include SMA deformation, SMA anchor displacement, and SMA pull-out) and (b) change in failure profile with SMA configuration.

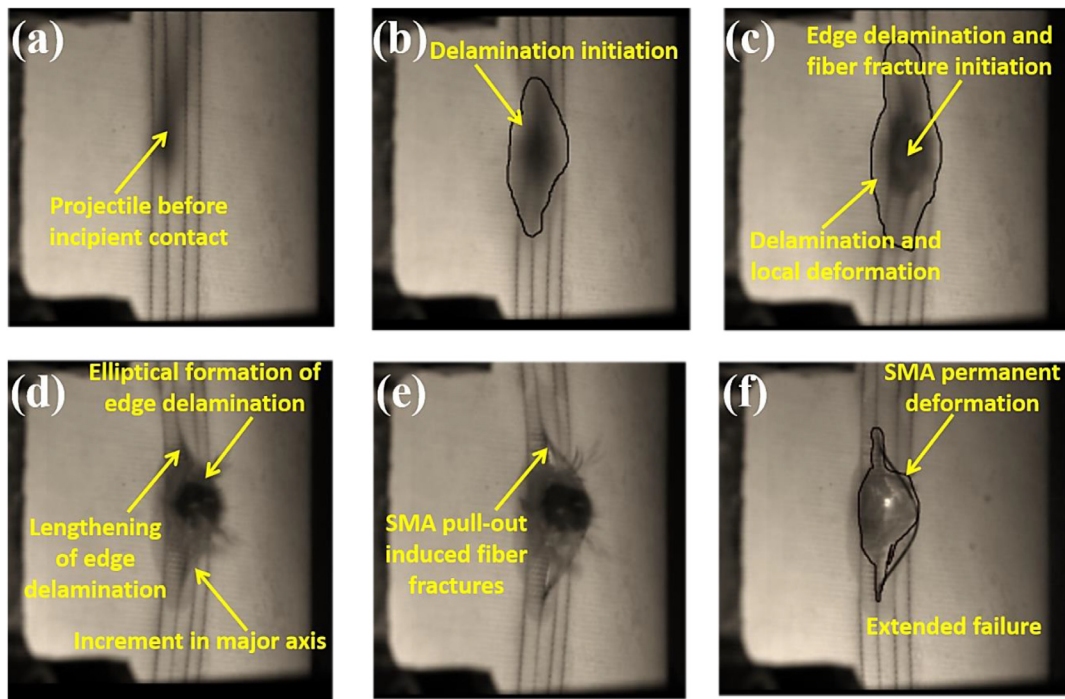


Fig. 5. (a-f) Sequence of images showing typical damage progression in a SMA embedded composite under high-velocity impact.

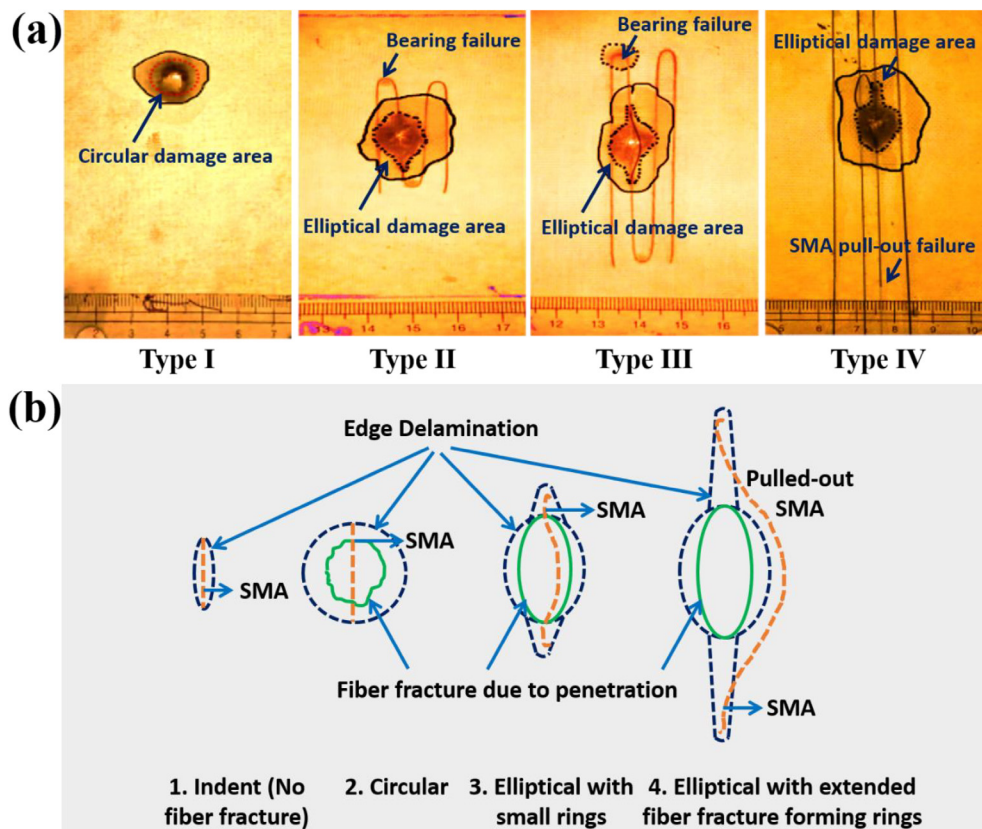


Fig. 6. (a) Post-impact photographic images showing typical damage profiles in different GFRP samples and (b) schematic of change in fiber fracture and edge delamination due to change in SMA pull-out. Either increase in velocity or SMA length changes extend of edge delamination and fiber fracture failure mode.

depend on the embedded SMA configuration. This factor leads to changes in the delamination area depending upon impact velocity and pull-out extent.

In Type II and III samples, due to the presence of anchors, SMA pull-out is highly restricted or constrained Fig. 6(a). SMA deformation in and around the primary impact region undergoes a higher amount

of strain because of anchors, as bonding between GFRP and PE-SMA wire is strong in the anchored area, as shown in Fig. 4. As the strain increases further in the wire, it reaches a limiting value beyond which anchors displace, indicating a bearing failure. The moment when anchor displacement failure mode takes place, SMA pull-out failure mode happens in the impact region. If SMA pull-out occurs, it will lead to a large amount of energy absorption. The reason is that pull-out is preceded by the SMA deformation and the anchor displacement.

As projectile penetrates further Fig. 5(c–f), due to the SMA pull-out, extended fiber fracture and edge delamination (Fig. 2S) take place in the primary impact zone and along the PE-SMA wire. This event leads to a change in the damage profile (aspect ratio) of the SMA embedded samples in comparison to that of the homogeneous GFRP ones. In the homogeneous GFRPs, the extend of edge delamination and fiber fracture depends on the projectile diameter and happens around the region fractured by the projectile. Edge delamination in Type I configuration is circular, as shown in Fig. 6. In contrast, in SMA embedded GFRPs, there is a shape change of edge delamination failure mode from circular to elliptical even before the pull-out. This shape change is due to an increase in edge delamination failure mode along the embedded SMA, termed as a major axis, as shown in Figs. 5 and 6.

The damage growth in the minor axis is very less in comparison to that in the major axis. Thus, leading to the formation of an elliptically shaped edge delamination. This delamination growth in the major axis is due to the contact of the projectile with SMA and its effort to pull-out the SMA. As the projectile leaves the sample, there is an SMA pull-out failure mode, which is visible as in Fig. 5(f), due to permanent damage encountered by SMA in the primary impact region. At the impact point, PE-SMA wire undergoes the maximum strain value leading to their permanent deformation or damage. This permanent deformation of the PE-SMA wire can be verified from the SEM image shown in Fig. 7.

3.2. Effect of employing anchors in embedded SMA on the overall delamination area

Fig. 8 depicts the post-impact photographic images of different GFRP samples impacted at velocities 70, 85, 95, and 105 m/s. These figures clearly show the effect of impact velocity and SMA configuration on the SMA pull-out and other major failure modes. The overall delamination area is affected when PE-SMA is embedded in GFRP, in comparison to the homogeneous GFRPs. In the Type I samples, the overall delamination area decreases with increasing impact velocity (Fig. 9), as it is maximum at 70 m/s and a minimum at 105 m/s. On the other hand, for the PE-SMA based samples, the overall delamination area increases with an increase in velocity. At higher impact velocities, SMA leads to an increase in damage due to the delamination induced by the pull-out. Moreover, PE-SMA configuration embedded

in a GFRP plays an important role in the overall pull-out length. Table 5 summarizes the average SMA pull-out length of different impacted GFRP samples calculated via the digital image processing technique. Among the PE-SMA based samples, the Type II samples show the least delamination area. This can be attributed to the small embedded PE-SMA length and placement of anchors near the primary impact region (so the pull-out length is less in Type II). As shown in Fig. 9 and Table 5, increasing embedment length across Type II to IV lead to an increase in pull-out. Thus, when strain increases, in Type III configuration, the anchor displaces much earlier than in Type II configuration, leading to an increase in pull-out length at the same velocity.

At 70 m/s, though projectile rebounded for Type II and III configurations, there is a permanent dent that is visible on PE-SMA wire (Fig. 8). Thus without getting pulled-out, the projectile permanently deformed the length of wire equal to the projectile diameter. The same is true for Type II at 85 m/s. Once, anchor displacement happens in any configuration, a further increase in velocity leads to a rise in the pull-out. For Type II configuration, impact velocities 70 m/s and 85 m/s are below the ballistic limit. At these velocities, much anchor displacements are not observed. But for Type III, the projectile penetrated at 85 m/s, and anchor displacement is observed. Thus, at the same velocity, anchor displacements change with SMA configuration. Also, at higher impact velocities, the anchor displacement due to pull-out is less for Type II. Due to this, the delamination area is smaller in Type II.

It has been observed that deformation in the PE-SMA wire is higher in the anchored configurations (Type II, III) in comparison to the unanchored ones (Type IV). The deformation in anchored configurations continues in the wire until it reaches a strain where the anchor cannot hold anymore inside the GFRP. For Type IV, as anchors are not there (embedded wire is straight and not connected) and the PE-SMA length is also higher, the wire displaces at a load value much less than that at which displacement of the anchored configuration can take place. This will lead to an increase in the pull-out length (easy to displace the wire from the GFRP) and perhaps decreases the energy absorption. With more pull-out length, damage in the sample due to interlaminar separation (delamination) of the layers increases (Fig. 8).

Thus, it can be said that, at higher velocities, in all the SMA based configurations the delamination area increases, while in Type I samples it decreases. The overall delamination area will decrease with a decrease in embedded SMA length at the same velocity. Among the PE-SMA embedded configuration, Type II is the most effective as the delamination area remains the minimum at all velocities.

3.3. Ballistic limit (penetration velocities)

Table 6 summarizes the residual velocity for different types of GFRP samples at various impact velocities 70, 85, 95, and 105 m/s.

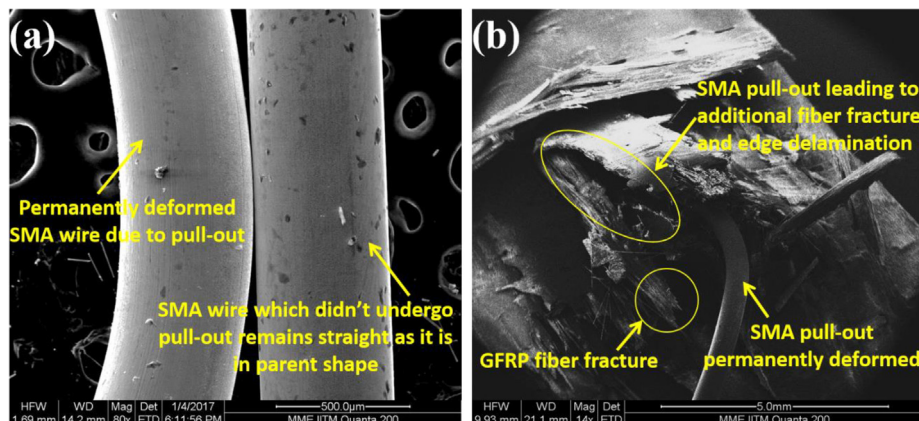


Fig. 7. SEM micrographs showing (a) typical SMA pull-out, and (b) different damage modes.

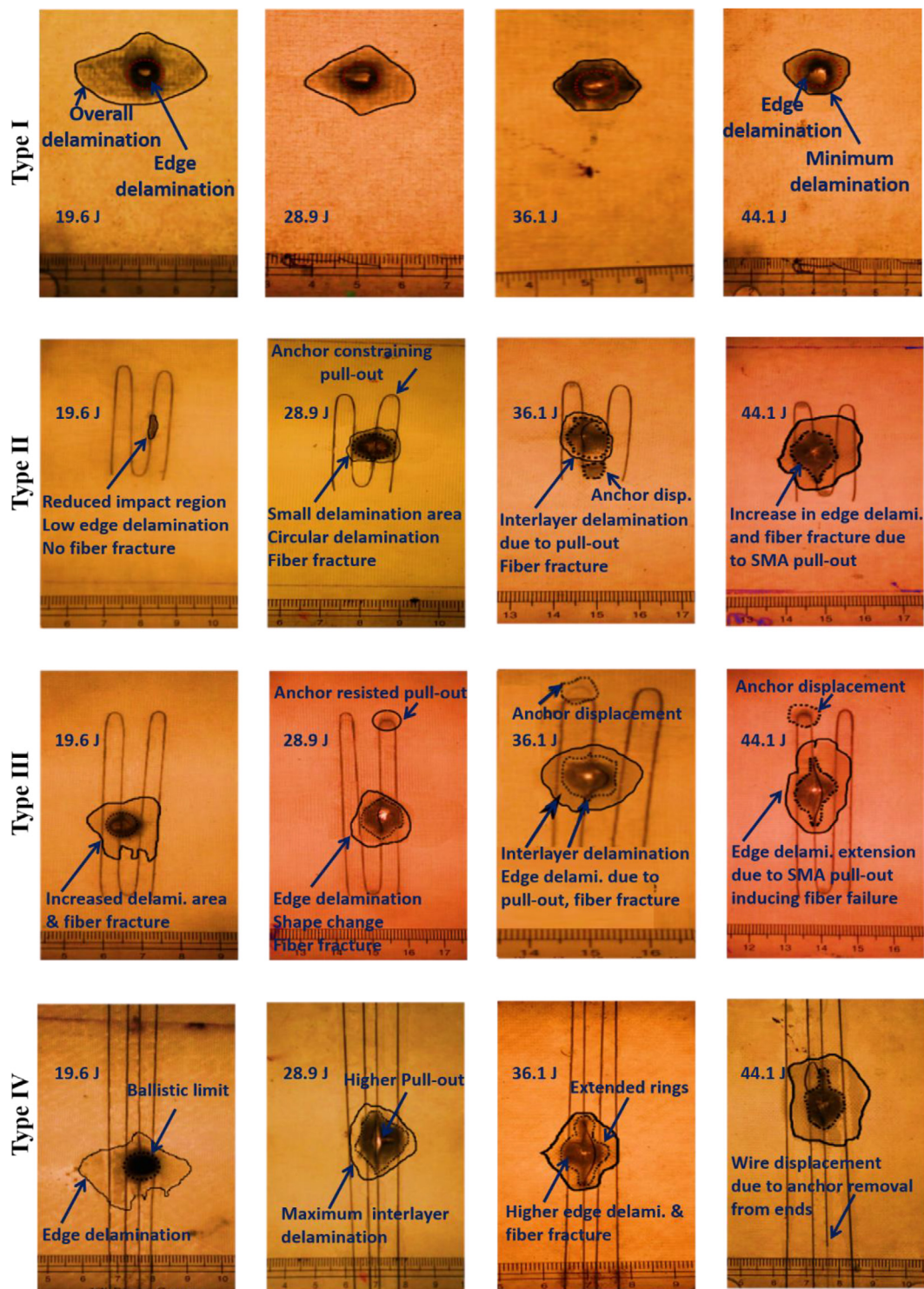


Fig. 8. Damage due to various failure modes in Type I, Type II, III and IV configurations at respective energy levels of velocity 70 m/s, 85 m/s, 95 m/s and 105 m/s. (Energy levels 19.6, 28.9, 36.1 and 44.1 J corresponds to impact velocities 70, 85, 95 and 105 m/s, respectively).

For the Type I sample, all the four impact velocities are above the ballistic limit. On the other hand, when PE-SMA wire is embedded, the ballistic limit increases. Besides, varying the embedment configuration, such as SMA length and presence of anchors, changed the ballistic limit. For Type II, Type III and Type IV samples, the ballistic limit is 95, 85, and 70 m/s, respectively, as the projectile rebounded (Fig. 8). These limits are significantly higher than that of Type I, where projectile penetration occurred at 55 m/s.

3.4. Total energy absorption

Fig. 10 shows the plot of absorbed energy versus velocity for different GFRP samples. The absorbed energy has been calculated by finding out the projectile velocity before and after the impact using a high-speed camera (the difference between the initial and residual kinetic energies) [42]. The ballistic limit for GFRP is estimated to be 55 m/s. At higher velocities, the amount of absorbed energy decreases.

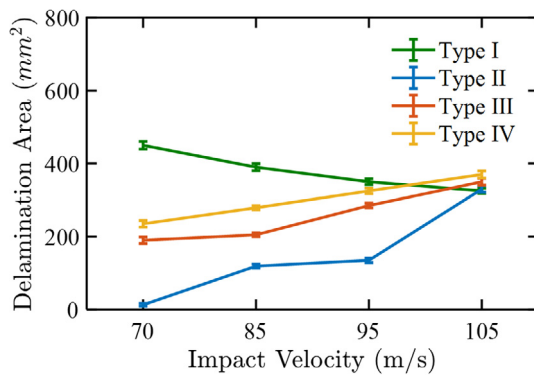


Fig. 9. Overall delamination area versus impact velocity plot for different GFRP samples impacted at velocities 70, 85, 95, and 105 m/s.

Table 5

Pull-out length in different SMA embedded configurations at different velocities.

S. No.	Velocity (m/s)	Pull out length (mm)		
		Type-II	Type-III	Type-IV
1	70	8	8	11
2	85	8	12	14
3	95	12	15	20
4	105	15	18	24

The reason behind this can be attributed to the decrease in the conventional failure modes such as delamination (i.e. more localized damage), as shown in Fig. 8. Embedding PE-SMA wire within GFRP leads to a relatively higher absorbed energy. At 70 m/s, the Type IV sample absorbs the maximum impact energy as it is the ballistic limit for the same. As impact velocity increased, the absorbed energy of the Type IV sample decreases (similar to Type I).

Unlike the Type IV sample, the absorbed energy increases from 70 to 105 m/s in Type II and Type III samples. The impact velocity 70 m/s is below the ballistic limit for both the configurations. At 85 m/s and above, the absorbed energy increases further because of the SMA pull-out (Fig. 8), in which anchors have to displace unlike Type IV. At 95 m/s and above, the absorbed energy of Type III was lower than that of Type II due to higher impact damage in the sample Fig. 8. As anchors are not present in Type IV samples, SMA pull-out failure mode happens easier in comparison to other PE-SMA wire embedded configurations. Hence, energy absorption in Type IV configuration is mini-

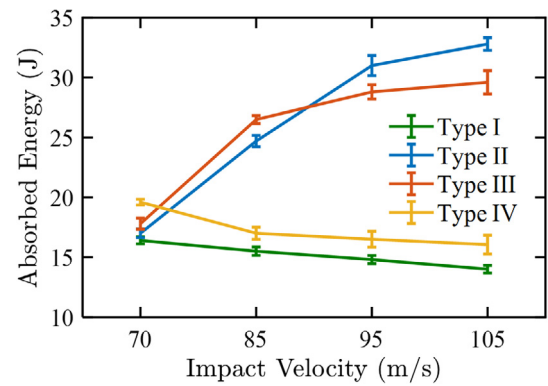


Fig. 10. Absorbed energy versus impact velocity plot for different GFRP samples impacted at velocities 70, 85, 95, and 105 m/s.

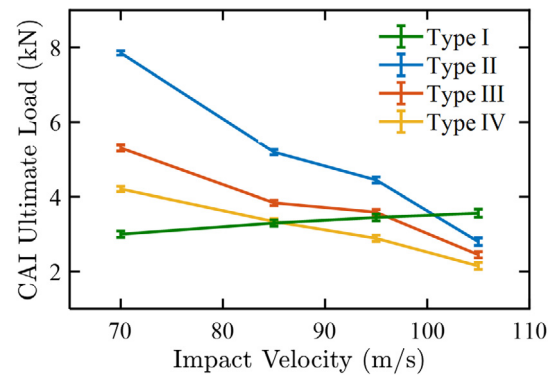


Fig. 11. Ultimate compression load versus impact velocity plot for different GFRP samples impacted at velocities 70, 85, 95, and 105 m/s.

imum among all the SMA based samples. With the help of these investigations, it can be concluded that the smaller the anchored embedment length, the higher will be the ballistic limit.

3.5. Compression after impact (CAI) test

During impact, when the PE-SMA wire is pulled out, failure modes such as fiber fracture and interlaminar separation near the region in which pull-out has taken place increases, as evident in Fig. 8. With an increase in these failure modes in and around the primary impact

Table 6

Rebound and residual velocities after high-velocity impact for different configurations.

Initial velocity (m/s)	Energy (J)	Sample No.	Residual velocity (m/s)			
			Type I	Type II	Type III	Type IV
70	19.6	1	27.56	26.25 (Rebound)	20.00 (Rebound)	0 (Ballistic limit)
		2	28.58	25.94 (Rebound)	22.20 (Rebound)	0 (Ballistic limit)
		3	28.89	25.25 (Rebound)	21.10 (Rebound)	0 (Ballistic limit)
		4	28.12	24.54 (Rebound)	21.20 (Rebound)	0.16 (Rebound)
85	28.9	1	57.56	31.90 (Rebound)	23.89	54.60
		2	57.20	32.50 (Rebound)	24.13	55.00
		3	58.84	33.68 (Rebound)	24.6	53.10
		4	57.90	32.39 (Rebound)	25.372	55.50
95	36.1	1	72.97	40.25	34.2	58.25
		2	73.3	43.75	37	57.67
		3	73.6	43.92	35.41	56.92
		4	72.02	42.95	36.2	60.00
105	44.1	1	87.54	52.00	51.90	67.42
		2	86.07	54.40	52.49	69.02
		3	86.92	52.60	50.70	65.17
		4	86.43	53.70	48.10	67.12

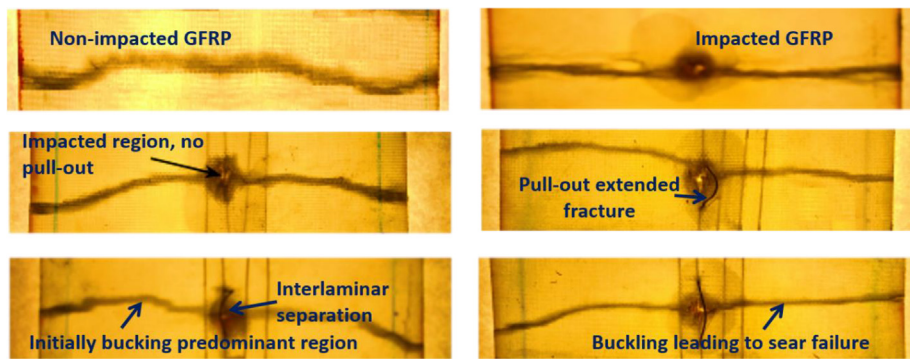


Fig. 12. Photographic images showing typical damage modes in different GFRP samples subjected to CAI test.

region, residual strength decreases. The role of different PE-SMA embedment on the residual strength of the impacted samples is evaluated via compression after impact (CAI) tests. The ultimate compression load of different samples at various impact velocities are shown in Figs. 11 and 12 show the post-impact compressive damage profile of different samples at various impact velocities.

For an impact velocity of 70 m/s, the projectile rebounds for Type II and III configurations (Fig. 8). Since the damage was smaller for Type II, the compressive strength is expected to be higher, as seen in Fig. 11. For the Type IV sample, the compressive strength is the lowest in comparison to the other two SMA based configurations. The reason is the maximum damage due to impact occurs in Type IV samples compared to Type II and Type III ones at the same impact velocity. With a further increase in the impact velocity, the compressive strength decreases for all three SMA configurations. This response is because of an increase in the number of operative failure modes, as explained earlier in Sections 3.1 and 3.2. The main factor determining the compressive strength is the intensity of failure modes in and around the primary impact region. For PE-SMA embedded samples, the SMA pull-out becomes a major factor in determining the compressive strength as it induces and exacerbates the failure modes such as interlaminar separation, fiber fracture, and edge delamination. Thus, the higher the pull-out length, the greater will be the interlayer separation (Fig. 12). Due to this interlayer separation, initiation of local buckling takes place from the primary impact region during compression (in all the impacted samples). On the other hand, for the Type I sample, the delamination area decreases at higher velocities, as shown in Fig. 8, leading to an increase in the compressive strength.

4. Conclusions

In this paper, the compression after high-velocity impact (CAI) behavior of pseudo-elastic shape memory alloy (PE-SMA) embedded glass/epoxy composite laminates manufactured via vacuum-assisted resin infusion (VARI) technique was studied experimentally. High-velocity impact tests were performed on the glass/epoxy composites at four different velocities (70, 85, 95, and 105 m/s). Three different types of embedment configurations of PE-SMA wire, namely, with length variation (35, 70, and 150 mm) and also with and without anchors, were used. This study presents the following important conclusions:

1. Embedding PE-SMA wire in GFRPs increases the ballistic limit. Besides, varying the embedment configuration, such as SMA length and presence of anchors, changed the ballistic limit. For Type II, Type III and Type IV samples, the ballistic limit is 95, 85, and 70 m/s, respectively. These limits are significantly higher than that of Type I, where projectile penetration occurred at 55 m/s.

2. At higher velocities, in all the SMA based configurations, the delamination area increases, while in the Type I samples, it decreases. At higher impact velocities, SMA leads to an increase in damage due to the delamination induced by the pull-out, while Type I samples show more localized damage.
3. An increase in the embedment length across Type II to IV leads to a raise increase in the overall delamination area at the same velocity. Among the PE-SMA embedded configuration, Type II is the most effective as the delamination area remains the minimum at all the impact velocities.
4. In Type II and III samples, due to the presence of anchors, SMA pull-out is highly restricted or constrained. SMA deformation in and around the primary impact region undergoes a higher amount of strain because of anchors, as bonding between GFRP and PE-SMA wire is strong in the anchored area.
5. For Type IV, as anchors are not there (embedded wire is straight and not connected) and the PE-SMA length is also higher, the wire displaces at a load value much less than that at which displacement of the anchored configuration can take place. This feature led to an increase in the pull-out length (easy to displace the wire from the GFRP), and thus decreases the energy absorption.
6. CAI results indicate that the PE-SMA based composites have better damage tolerance with respect to the homogeneous ones at 70 m/s. In contrast, at higher velocities, the delamination area decreases in the homogenous glass/epoxy composites due to more localized damage and present a higher compressive strength.

Declaration of Competing Interest

The authors declare that they have no known competing financial interests or personal relationships that could have appeared to influence the work reported in this paper.

Appendix A. Supplementary data

Supplementary data to this article can be found online at <https://doi.org/10.1016/j.compstruct.2020.113519>.

References

- [1] Andrew JJ, Srinivasan SM, Arockiarajan A, Dhakal HN. Parameters influencing the impact response of fiber-reinforced polymer matrix composite materials: A critical review. *Compos Struct* 2019;224:111007. <https://doi.org/10.1016/j.compstruct.2019.111007>.
- [2] Mata-Díaz A, López-Puente J, Varas D, Pernas-Sánchez J, Artero-Guerrero JA. Experimental analysis of high velocity impacts of composite fragments. *Int J Impact Eng* 2017;103:231–40. <https://doi.org/10.1016/j.ijimpeng.2017.01.013>.
- [3] Sutherland LS. A review of impact testing on marine composite materials: Part I – Marine impacts on marine composites. *Compos Struct* 2018;188:197–208. <https://doi.org/10.1016/j.compstruct.2017.12.073>.

- [4] Jefferson Andrew J, Arumugam V, Saravanakumar K, Dhakal HN, Santulli C. Compression after impact strength of repaired GFRP composite laminates under repeated impact loading. *Compos Struct* 2015;133:911–20. <https://doi.org/10.1016/j.compstruct.2015.08.022>.
- [5] Jefferson AJ, Srinivasan SM, Arockiarajan A. Effect of multiphase fiber system and stacking sequence on low-velocity impact and residual tensile behavior of glass/epoxy composite laminates. *Polym. Compos.* 2019;40(4):1450–62. <https://doi.org/10.1002/pc.24884>.
- [6] Reddy PRS, Reddy TS, Madhu V, Gogia AK, Rao KV. Behavior of E-glass composite laminates under ballistic impact. *Mater Des* 2015;84:79–86. <https://doi.org/10.1016/j.matdes.2015.06.094>.
- [7] Sudhir Sastry YB, Budarapu PR, Krishna Y, Devaraj S. Studies on ballistic impact of the composite panels. *Theor Appl Fract Mech* 2014;72:2–12. <https://doi.org/10.1016/j.tafmec.2014.07.010>.
- [8] Hu D, Zhang C, Ma X, Song B. Effect of fiber orientation on energy absorption characteristics of glass cloth/epoxy composite tubes under axial quasi-static and impact crushing condition. *Compos A Appl Sci Manuf* 2016;90:489–501. <https://doi.org/10.1016/j.compositesa.2016.08.017>.
- [9] Jefferson Andrew J, Srinivasan SM, Arockiarajan A. The role of adhesively bonded super hybrid external patches on the impact and post-impact response of repaired glass/epoxy composite laminates. *Compos Struct* 2018;184:848–59. <https://doi.org/10.1016/j.compstruct.2017.10.070>.
- [10] Balaganesan, G., et al. "Energy-Absorbing Capacity of Polyurethane/SiC/Glass-Epoxy Laminates Under Impact Loading." *Journal of Engineering Materials and Technology* 139.2 (2017): 021008.
- [11] Bhoominathan R, Arumugam V, Ashok T, Jefferson AJ. Residual strength estimation of CFRP laminates subjected to impact at different velocities and temperatures. *Polym Compos* 2017;38(10):2182–91. <https://doi.org/10.1002/pc.23796>.
- [12] Andrew J, Ramesh C. Residual strength and damage characterization of unidirectional glass-basalt hybrid/epoxy CAI Laminates. *Arab J Sci Eng* 2015;40(6):1695–705. <https://doi.org/10.1007/s13369-015-1651-8>.
- [13] Moallemzadeh AR, Sabet SAR, Abedini H. Preloaded composite panels under high velocity impact. *Int J Impact Eng* 2018;114:153–9. <https://doi.org/10.1016/j.ijimpeng.2017.12.019>.
- [14] Paine, Jeffrey SN, and Craig A. Rogers. "The response of SMA hybrid composite materials to low velocity impact." *Journal of Intelligent Material Systems and Structures* 5.4 (1994): 530–535.
- [15] Paine, Jeffrey SN, and Craig A. Rogers. "Shape memory alloys for damage-resistant composite structures." *Active materials and smart structures*. Vol. 2427. International Society for Optics and Photonics, 1995.
- [16] Tsoi KA, Stalmans R, Schrooten J, Wevers M, Mai Y-W. Impact damage behaviour of shape memory alloy composites. *Mater Sci Eng, A* 2003;342(1-2):207–15. [https://doi.org/10.1016/S0921-5093\(02\)00317-9](https://doi.org/10.1016/S0921-5093(02)00317-9).
- [17] Nallathambi AK et al. A 3-species model for shape memory alloys. *Int J Struct Changes Solids* 2009;1(1):149–70.
- [18] Auricchio F, Petrini L. A three-dimensional model describing stress-temperature induced solid phase transformations: solution algorithm and boundary value problems. *Int J Numer Meth Eng* 2004;61(6):807–36. <https://doi.org/10.1002/nme.1086>.
- [19] Verma L, Sivakumar SM, Vedantam S. Homogenization and improvement in energy dissipation of nonlinear composites. *SPIE Smart Structures and Materials + Nondestructive Evaluation and Health Monitoring*. International Society for Optics and Photonics; 2016.
- [20] Wei ZG, Sandstrom R, Miyazaki S. Shape memory materials and hybrid composites for smart systems: Part II Shape-memory hybrid composites. *J Mater Sci* 1998;33(15):3763–83.
- [21] Meo M et al. Shape memory alloy hybrid composites for improved impact properties for aeronautical applications. *Compos Struct* 2013;95:756–66.
- [22] Angioni SL, Meo M, Foreman A. Impact damage resistance and damage suppression properties of shape memory alloys in hybrid composites – A review. *Smart Mater Struct* 2010;20(1):013001.
- [23] Ali MAEM, Soliman AM, Nehdi ML. Hybrid-fiber reinforced engineered cementitious composite under tensile and impact loading. *Mater Des* 2017;117:139–49.
- [24] Jani, Jaronie Mohd, et al. "A review of shape memory alloy research, applications and opportunities." *Materials & Design* (1980-2015) 56 (2014): 1078–1113.
- [25] Wu Y et al. Study on the response to low-velocity impact of a composite plate improved by shape memory alloy. *Acta Mech Solida Sin* 2007;20(4):357–62.
- [26] Kim E-H et al. Effects of shape memory alloys on low velocity impact characteristics of composite plate. *Compos Struct* 2011;93(11):2903–9.
- [27] Paine J, Rogers C. High velocity impact response of composites with surface bonded nitinol-SMA hybrid layers. 36th Struct Struct Dyn Mater Conf 1995.
- [28] Kiesling T et al. Impact failure modes of thin graphite epoxy composites embedded with superelastic nitinol. 37th Struct Struct Dyn Mater Conf 1996.
- [29] Lau K-T, Ling H-Y, Zhou L-M. Low velocity impact on shape memory alloy stitched composite plates. *Smart Mater Struct* 2004;13(2):364.
- [30] Amano M, Okabe Y, Takeda N. Evaluation of crack suppression effect of TiNi SMA foil embedded in CFRP cross-ply laminates with embedded small-diameter FBG sensor. *JSMIE Int J Series A Solid Mech Mater Eng* 2005;48(4):443–50.
- [31] Neuking K, Abu-Zarifa A, Eggeler G. Surface engineering of shape memory alloy/polymer-composites: Improvement of the adhesion between polymers and pseudoelastic shape memory alloys. *Mater Sci Eng, A* 2008;481:606–11.
- [32] Murkute V et al. "Improvisation of interfacial bond strength in shape memory alloy hybrid polymer matrix composites." *Procedia. Mater Sci* 2014;6:316–21.
- [33] Abir MR et al. On the relationship between failure mechanism and compression after impact (CAI) strength in composites. *Compos Struct* 2017;182:242–50.
- [34] Berkettis K, Tzetzis D, Hogg PJ. The influence of long term water immersion ageing on impact damage behaviour and residual compression strength of glass fibre reinforced polymer (GFRP). *Mater Des* 2008;29(7):1300–10.
- [35] Bhatia GS, Jefferson Andrew J, Arockiarajan A. Experimental investigation on compressive behaviour of different patch-parent layup configurations for repaired carbon/epoxy composites. *J Compos Mater* 2019;53(23):3269–79.
- [36] Koo J-M, Choi J-H, Seok C-S. Prediction of post-impact residual strength and fatigue characteristics after impact of CFRP composite structures. *Compos B Eng* 2014;61:300–6.
- [37] Rivalent S et al. Experimental analysis of CFRP laminates subjected to compression after impact: The role of impact-induced cracks in failure. *Compos Struct* 2014;111:147–57.
- [38] Aslan Z, Şahin M. Buckling behavior and compressive failure of composite laminates containing multiple large delaminations. *Compos Struct* 2009;89(3):382–90.
- [39] Chen H, Sun X. Residual compressive strength of laminated plates with delamination. *Compos Struct* 1999;47(1-4):711–7.
- [40] Evci C, Gülgeç M. An experimental investigation on the impact response of composite materials. *Int J Impact Eng* 2012;43:40–51.
- [41] Yashiro S et al. Characterization of high-velocity impact damage in CFRP laminates: Part I-Experiment. *Compos A Appl Sci Manuf* 2013;48:93–100.
- [42] Verma L, Sivakumar SM, Jefferson J, Andrew G, Balaganesan AA, Vedantam S. Compression after ballistic impact response of pseudoelastic shape memory alloy embedded hybrid unsymmetrical patch repaired glass-fiber reinforced polymer composites. *J Compos Mater* 2019;53(28–30):4225–47.